Diachronous Redistribution of Hf and Nd Isotopes at the Crystal Scale-Consequences for the Isotopic Evolution of a Poly-Metamorphic Crustal Terrane

Adrien Vezinet, Emilie Thomassot, Chiranjeeb Sarkar, D. Graham Pearson, Yan Luo

▶ **To cite this version:**

Adrien Vezinet, Emilie Thomassot, Chiranjeeb Sarkar, D. Graham Pearson, Yan Luo. Diachronous Redistribution of Hf and Nd Isotopes at the Crystal Scale-Consequences for the Isotopic Evolution of a Poly-Metamorphic Crustal Terrane. Geosciences, 2022, 12 (1), pp.36. 10.3390/geosciences12010036 . hal-03539415

HAL Id: hal-03539415
https://hal.science/hal-03539415

Submitted on 22 Jan 2022

HAL is a multi-disciplinary open access archive for the deposit and dissemination of scientific research documents, whether they are published or not. The documents may come from teaching and research institutions in France or abroad, or from public or private research centers.

L'archive ouverte pluridisciplinaire **HAL**, est destinée au dépôt et à la diffusion de documents scientifiques de niveau recherche, publiés ou non, émanant des établissements d'enseignement et de recherche français ou étrangers, des laboratoires publics ou privés.

Distributed under a Creative Commons Attribution 4.0 International License

geosciences

MDPI

Article

Diachronous Redistribution of Hf and Nd Isotopes at the Crystal Scale—Consequences for the Isotopic Evolution of a Poly-Metamorphic Crustal Terrane

Adrien Vezinet [1,2,*], Emilie Thomassot [3], Yan Luo [1], Chiranjeeb Sarkar [1] and D. Graham Pearson [1]

[1] Department of Earth and Atmospheric Sciences, University of Alberta, Edmonton, AL T6G 2E3, Canada; yluo4@ualberta.ca (Y.L.); chiranjeeb.sarkar@ualberta.ca (C.S.); gdpearso@ualberta.ca (D.G.P.)
[2] University Grenoble Alpes, University Savoie Mont Blanc, CNRS, IRD, University Gustave Eiffel, ISTerre, 38000 Grenoble, France
[3] Centre de Recherches Pétrographiques et Géochimiques (CRPG), UMR 7358, Université de Lorraine, CNRS, 54501 Vandœuvre-lès-Nancy, France; emilie.thomassot@univ-lorraine.fr
* Correspondence: adrien.vezinet@univ-grenoble-alpes.fr

Abstract: In metamorphic rocks, mineral species react over a range of pressure–temperature conditions that do not necessarily overlap. Mineral equilibration can occur at varied points along the metamorphic pressure–temperature (PT) path, and thus at different times. The sole or dominant use of zircon isotopic compositions to constrain the evolution of metamorphic rocks might then inadvertently skew geological interpretations towards one aspect or one moment of a rock's history. Here, we present in-situ U–Pb/Sm–Nd isotope analyses of the apatite crystals extracted from two meta-igneous rocks exposed in the Saglek Block (North Atlantic craton, Canada), an Archean metamorphic terrane, with the aim of examining the various signatures and events that they record. The data are combined with published U–Pb/Hf/O isotope compositions of zircon extracted from the same hand-specimens. We found an offset of nearly *ca.* 1.5 Gyr between U-Pb ages derived from the oldest zircon cores and apatite U–Pb/Sm–Nd isotopic ages, and an offset of *ca.* 200 Ma between the youngest zircon metamorphic overgrowths and apatite. These differences in metamorphic ages recorded by zircon and apatite mean that the redistribution of Hf isotopes (largely hosted in zircon) and Nd isotopes (largely hosted in apatite within these rocks), were not synchronous at the hand-specimen scale ($\leq$~0.001 m^3). We propose that the diachronous redistribution of Hf and Nd isotopes and their parent isotopes was caused by the different PT conditions of growth equilibration between zircon and apatite during metamorphism. These findings document the latest metamorphic evolution of the Saglek Block, highlighting the role played by intra-crustal reworking during the late-Archean regional metamorphic event.

Keywords: apatite U–Pb/Sm–Nd isotopes; metamorphism; Archean Saglek; Hf–Nd decoupling

check for updates

Citation: Vezinet, A.; Thomassot, E.; Luo, Y.; Sarkar, C.; Pearson, D.G. Diachronous Redistribution of Hf and Nd Isotopes at the Crystal Scale—Consequences for the Isotopic Evolution of a Poly-Metamorphic Crustal Terrane. *Geosciences* **2022**, *12*, 36. https://doi.org/10.3390/geosciences12010036

Academic Editors: José Manuel Castro and Jesus Martinez-Frias

Received: 30 November 2021
Accepted: 10 January 2022
Published: 12 January 2022

Publisher's Note: MDPI stays neutral with regard to jurisdictional claims in published maps and institutional affiliations.

Copyright: © 2022 by the authors. Licensee MDPI, Basel, Switzerland. This article is an open access article distributed under the terms and conditions of the Creative Commons Attribution (CC BY) license (https://creativecommons.org/licenses/by/4.0/).

1. Introduction

Combining the various isotope systematics accessible in zircon ($ZrSiO_4$), such as U-Pb and Lu-Hf isotopes, has become a classical means for studying the crustal remnants exposed in early-Archean terranes (e.g., [1–5]). Zircon U–Th–Pb/Hf/O isotope compositions are also largely used to depict the compositional evolution of the terrestrial crust through time (e.g., [6,7]), and build tectonic models for the early Earth [8] and references therein. The primary geological features of the oldest geological archives have, however, been largely erased due to several stages of metamorphism. Zircon chemical and isotopic compositions then reflect only one aspect of a broader, and in some instances protracted, story. Using solely these compositions might introduce bias in models for the Hadean/Archean evolution.

Complementary information can be obtained from the study of rare earth element (REE)-rich minerals, such as apatite, titanite and, monazite [9] which, in addition to hosting trace elements that can be used to discriminate their origin [10], can host appreciable amounts of radioactive U, Th and Sm, which result in measurable amounts of radiogenic Pb and Nd with laser ablation protocols (e.g., [11–14]). These properties, and the relatively high reactivity of REE-rich minerals during metamorphism, make these minerals well-suited to providing more definite constraints on the timing and conditions of metamorphic processes [15–20].

In Archean terranes, where a large majority of rocks have experienced poly-metamorphic histories, the reliability of whole-rock Lu–Hf and Sm–Nd isotope compositions to reflect the primary, igneous, signature, has been questioned [21–24]. The same applies to the latest metamorphic event: it is unlikely that whole-rock isotopic compositions fully encapsulate the effect of metamorphism on isotopic signatures. Spatially resolved techniques combined with time-resolved data treatment circumvent, at least partly, the pitfalls encountered in whole-rock isotopes analyses, such as the averaging of varied rock components that have responded in different ways to multiple metamorphic events. Studies of U–Th–Pb ± Sm–Nd isotope systematics, produced with spatially resolved analytical techniques, have provided more comprehensive views of the evolution of magmatic and metamorphic systems [16,19,25,26], especially when isotopic compositions of zircon and REE-rich minerals from the same rock are integrated [27–30]. The latter approach is the one used in this study.

We present U–Th–Pb/Sm–Nd isotope measurements of apatite, a phosphate of the hexagonal crystal system $Ca_5(PO_4)_3(F,OH,Cl)$, from two meta-igneous rocks from the Archean Saglek Block (Figure 1) and their corresponding whole-rock Sm–Nd isotopes compositions. Apatite isotope analyses were produced with the laser ablation split stream (LASS) protocol detailed in [28], ensuring perfect matching between U–Pb and Sm–Nd isotope ratio measurements. The two metamorphic rocks investigated here have known zircon U–Th–Pb/Hf/O isotope compositions, making these samples suitable for discussing the significance of varied isotope systematics at both the crystal and the whole-rock scale in metamorphic systems. The antiquity of the geological terrane they reside in—the Saglek Block, North Atlantic Craton—make the implications of these results relevant to models for the development of geochemical reservoirs in Hadean/Archean times.

2. The Saglek Block, an Archean Poly-Metamorphic Terrane

The Saglek Block is an Archean metamorphic terrane that forms the western part of the North Atlantic craton (Figure 1A,B). This terrane hosts lithologies broadly similar in age and chemical composition to the meta-igneous and meta-sedimentary lithologies from the Itsaq Gneiss Complex and the Isua supracrustal belt exposed in south-western Greenland [31,32]. The Saglek Block experienced high temperature metamorphic events, attaining conditions up to granulite facies, locally associated with partial melting [33]. Three metamorphic events have been recognized, scattered through the Archean and the early Proterozoic, at *ca.* 3.6 Ga, *ca.* 2.8–2.7 Ga and, *ca.* 2.5–2.4 Ga, referred to as M1, M2 and, M3, respectively, in the following. In addition to field and petrographic evidence, these three metamorphic events have been identified via isotopic measurements at the whole-rock scale [31,34–37] and further confirmed by U–Th–Pb isotope analyses of accessory minerals [38–45], sometimes combined with Hf-isotopes [28,46], Hf- and O-isotopes [5,47], and Sm–Nd isotopes [28,30].

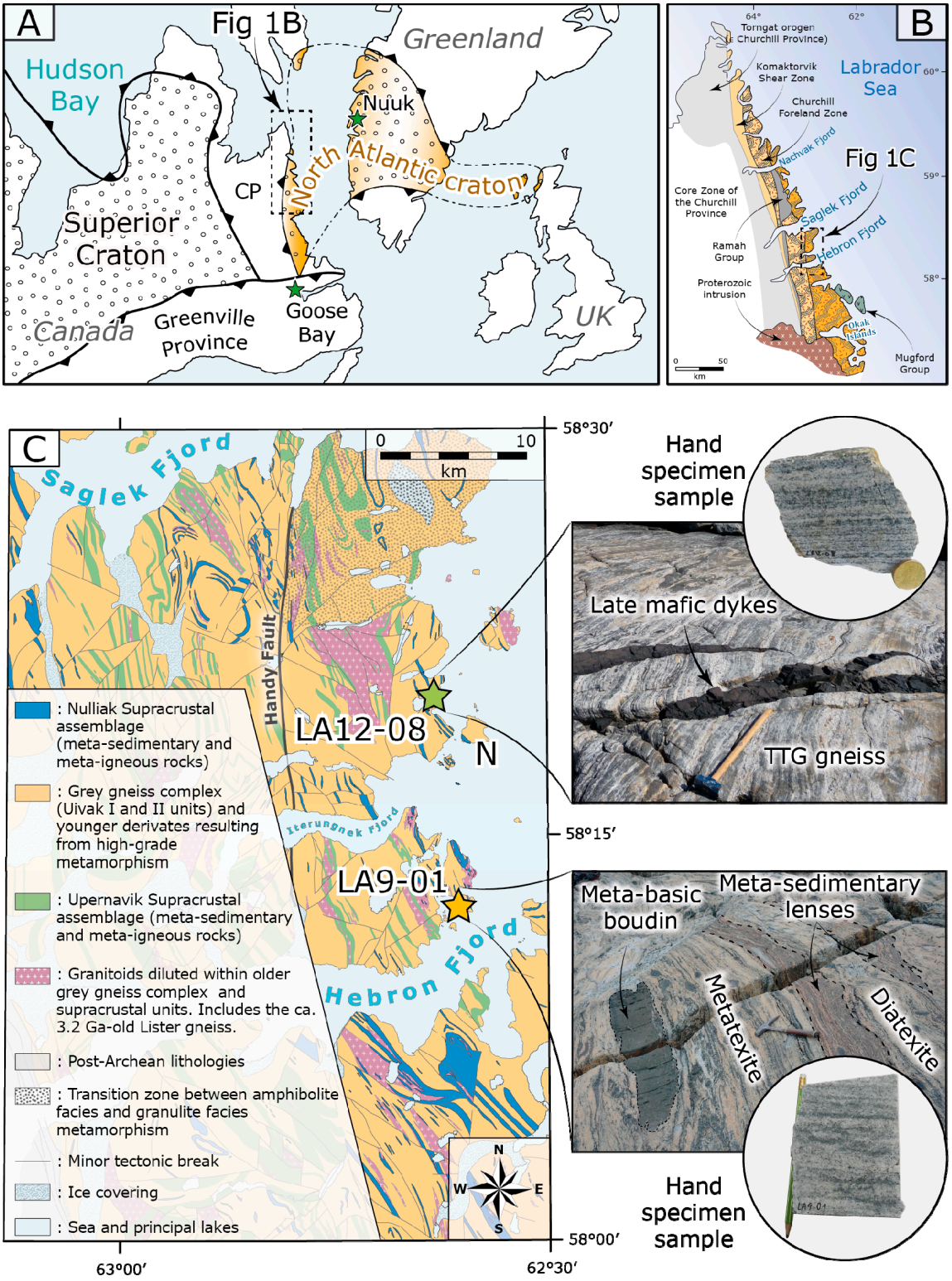

Figure 1. (**A**) Pre-drift reconstruction of the North Atlantic craton (yellow area on the map), dotted areas are pre-2.5 Ga terranes; green stars represent towns. CP: Churchill Province. (**B**) General geological map of the north-eastern Labrador and Québec modified after [modified after 48]. (**C**) Geological map of the Saglek Block modified after [48], with localization of the sampling sites (green and yellow stars), and a view of the outcrops and hand-specimens investigated in this study. N: Nulliak Island. Star color coding does not refer to lithology.

Exploratory U–Th–Pb isotope compositions of REE-rich minerals were presented in [43] and have recently been complemented with modern spatially resolved techniques [28,30,39,40]. All these studies point toward a metamorphic origin for REE-rich minerals in the Saglek Block and late-Neoarchean to early-Paleoproterozoic (re)-crystallization ages. Studies reporting combined U–Th–Pb/Sm–Nd isotope compositions [28,30] indicate the significant deviation of chondritic values [49] toward negative values at the time of crystallization: $\leq ca. -10$ ε. Here, we complement these studies to further resolve the events contributing to the metamorphic evolution of the Archean Saglek Block and the early Earth.

3. Methods

3.1. Sampling Strategy

The two gneisses investigated here have been characterized in previous studies. Only key aspects are reported here. Sample LA12-08, investigated in [5], is a Bt-bearing grey gneiss sampled on the shore facing Nulliak Island (Figure 1). This sample consisted of Pl + Qz + Bt + Zrn + Ap + Spn abbreviation after [50], and featured nascent mineral segregation (Figure 1). No high temperature phase, such as Gt or Opx, was present in this sample. Sample LA12-08 was selected as representing a felsic igneous rock in the area that was least modified by metamorphism since magma crystallization. Sample LA12-08 will be referred to as the "amphibolite facies grey gneiss". Sample LA9-01, investigated in [47], was collected from an outcrop made of strongly deformed felsic phaneritic material, associated with diatexitic material (Figure 1). The mineral assemblage of LA9-01 was similar to the assemblage observed in LA12-08, although Gt-bearing metasediments, interpreted as indicating granulite facies conditions of metamorphism, surrounded the LA9-01 sample site. Sample LA9-01 was selected to unfold the effects of the regional metamorphic events onto felsic members of the local grey gneiss suite, and will be referred to as the "metatexite". Both samples are meta-igneous rocks that show major and trace element chemistry similar to typical TTG suites worldwide [5,47].

3.2. Apatite U–Pb/Sm–Nd LASS Analyses

Apatite grains were hand-picked, mounted in an epoxy mount and polished, following standard techniques. Back-scattered electron (BSE, Figure 2) images were obtained before laser ablation analysis. Apatite U–Th–Pb/Sm–Nd LASS analyses were conducted in the Arctic Resource Geochemistry Laboratory (University of Alberta, Canada) following the procedure presented in [28]. In order to select a spot size relevant for our apatite populations, trace element analyses were conducted to evaluate U, Pb, Sm and, Nd elemental contents before LASS analyses. For LASS analyses, a nominal spot size of 130 µm was used. U–Th–Pb isotopes were measured on a Thermo-Fisher Scientific *Element XR* SC–ICP–MS, whereas Sm–Nd isotopes were measured on a Thermo-Fisher Scientific *Neptune Plus* MC–ICP–MS. Bancroft apatite refered to as "Tory Hill" in [28] was used as a calibration reference material for both U–Th–Pb and Sm–Nd isotope measurements, whereas Durango [28,51] and Mud Tank apatite were used as validation reference materials. U–Th–Pb and Sm–Nd ratios obtained on validation reference materials overlapped with the accepted values (see Supplementary data Table S1).

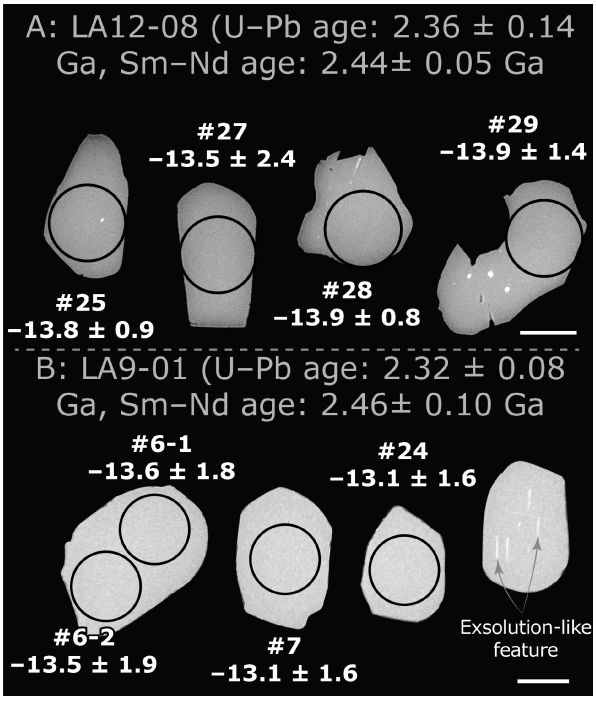

Figure 2. Representative BSE images of apatite crystals from the amphibolite facies grey gneiss LA12-08 (panel **A**) and metatexite LA9-01 (panel **B**). Scale bars represent 100 µm. Spot size: 130 µm. Labels represent analysis number (#) and $\varepsilon^{143}Nd_{initial}$ deviation ± uncertainty at 95% confidence level calculated at the Sm–Nd isochron apparent age for each apatite population.

3.3. Whole-Rock Sm–Nd Isotope Analyses

A known amount of pre-calibrated ^{150}Nd-^{149}Sm spike was added to each fraction prior to dissolution by a mixture of conc. HF (48%) and HNO_3 (16 N) in a 2:1 ratio on a hotplate at 120 °C for 48–72 h. This stage was repeated 3 times for each sample. The solution was evaporated to dryness before being converting into chloride form to pass through the column chemistry. Nd and Sm were separated from other REE and major elements using a cation column (AG 50 W X8 200–400 mesh) followed by a Ln spec column chemistry, following a similar procedure as described by [52].

Following column chromatography, chemically purified Sm and Nd fractions were dried and re-dissolved into 1 mL of a 2% nitric acid solution. Nd and Sm isotopic compositions were measured from these solutions using a Neptune *Plus* ICP-MS at the Arctic Resources Geochemistry Laboratory (University of Alberta, Canada). Nd isotopes were measured in static mode for 60 ratios of 8 s duration, whereas 30 Sm ratios were measured with 4 s integrations. The mass fractionation of Nd isotopes was exponentially corrected by applying an ^{146}Nd/^{144}Nd ratio of 0.7219, outlined by [53]. The ^{149}Sm signal was monitored and the invariant ratio of ^{149}Sm/^{144}Sm was used to correct for any isobaric interference of Sm on ^{144}Nd. A 100-ppb solution of JNdi-1 was used as a primary standard, measured repeatedly throughout the session. An average of 15 measurements of the JNdi-1 yielded a value of 0.512088 ± 0.000014 (2 SD, n = 15) and 0.512072 ± 0.000020 (2 SD, n = 15) for each analytical run. Both average values were in agreement with the accepted value [54]. In addition to the primary standards analyzed, two replicates of the Hawaiian basalt standard BHVO-2 were processed alongside each analytical batch as a secondary standard. Sm–Nd isotopes ratios obtained on BHVO-2 were within the uncertainty of accepted values. See [54] for the reference values.

3.4. Uncertainty in Isotopic Ratio and Values Derived from It

Chronological and compositional information calculated from our apatite U–Pb/Sm–Nd isotope analyses were obtained with the IsoplotR freeware version 993/629 [55]. All regressions were calculated using the Maximum Likelihood Estimation (MLE) algorithm available in IsoplotR. Decay constants for uranium U and Sm were default values input in IsoplotR version 993/629 [55]: 0.000155125 Myr^{-1} for ^{238}U, 0.00098485 Myr^{-1} for ^{235}U and 0.00000654 Myr^{-1} for ^{147}Sm. In cases where the MSWD value of the MLE regression was within the acceptable range at the 95% confidence level, as defined in [56], the uncertainty reported was y: "the studentized 95% confidence interval using the appropriate number of degrees of freedom". Where the MSWD value of the MLE regression was not within the acceptable range at 95% confidence level, the uncertainty reported was z: "the approximate 95% confidence interval with overdispersion, calculated as $z = y \times \sqrt{MSWD}$". For all regressions presented here, external (systematic) uncertainties were propagated in final ages and initial ratios. Epsilon (ε) deviations of initial isotopic ratios were obtained with the Model-1 algorithm of [57]. Two levels of uncertainty in the ε value were reported: (i) neglecting uncertainty in both the CHUR model and the decay constant, and (ii) propagating uncertainty in both the CHUR model and the decay constant. These two levels were reported along with the ε value and separated by a vertical bar ("|" symbol). In the discussion section, only the second is reported. Uncertainty in the age is included in both calculations.

4. Results

Apatite U–Pb/Sm–Nd isotopes and whole-rock Sm–Nd isotope results are presented in Table 1, Table 2 and Figure 3 Analyses of the validation reference materials (Durango and Mud Tank apatite) are reported in the SI, and are within the uncertainty of the accepted values. Individual data point uncertainty in Pb–Pb isotopes ratios had a mean of 4.7% (2SE). Individual data point uncertainty in the $^{143}Nd/^{144}Nd$ value had a mean of 0.6 ε (2SE).

Table 1. Summary of the apatite U–Pb/Sm–Nd LASS analyses conducted in this study. Elemental contents are reported in part per million and were measured before LASS analyses (n = 5 for each apatite population). Uncertainty is reported at 95% confidence level. Initial epsilon (ε) deviations were calculated following the Model-1 algorithm of [57] and include uncertainty in apparent age, CHUR model and decay constant. Corresponding Pb–Pb and Sm–Nd isochron diagrams are displayed in Figure 3.

	Th	**U**	**Pb**	**Sm**	**Nd**	**Pb–Pb Age ± Uncertainty (Ma)**	**MSWD**	***n***	**Sm–Nd Age ± Uncertainty (Ma)**	**MSWD**	***n***	$\varepsilon^{143}Nd_{initial}$
Amph. facies grey gneiss LA12-08	0.3	2.6	3.7	244	800	2359 ± 139	1.2	32 (/34)	2442 ± 50	1.2	33 (/34)	−13.7 ± 1.7
Metatexite LA9-01	14.6	7.1	5.6	175	1075	2318 ± 75	0.69	42 (/42)	2462 ± 104	1.1	38 (/42)	−13.2 ± 3.1

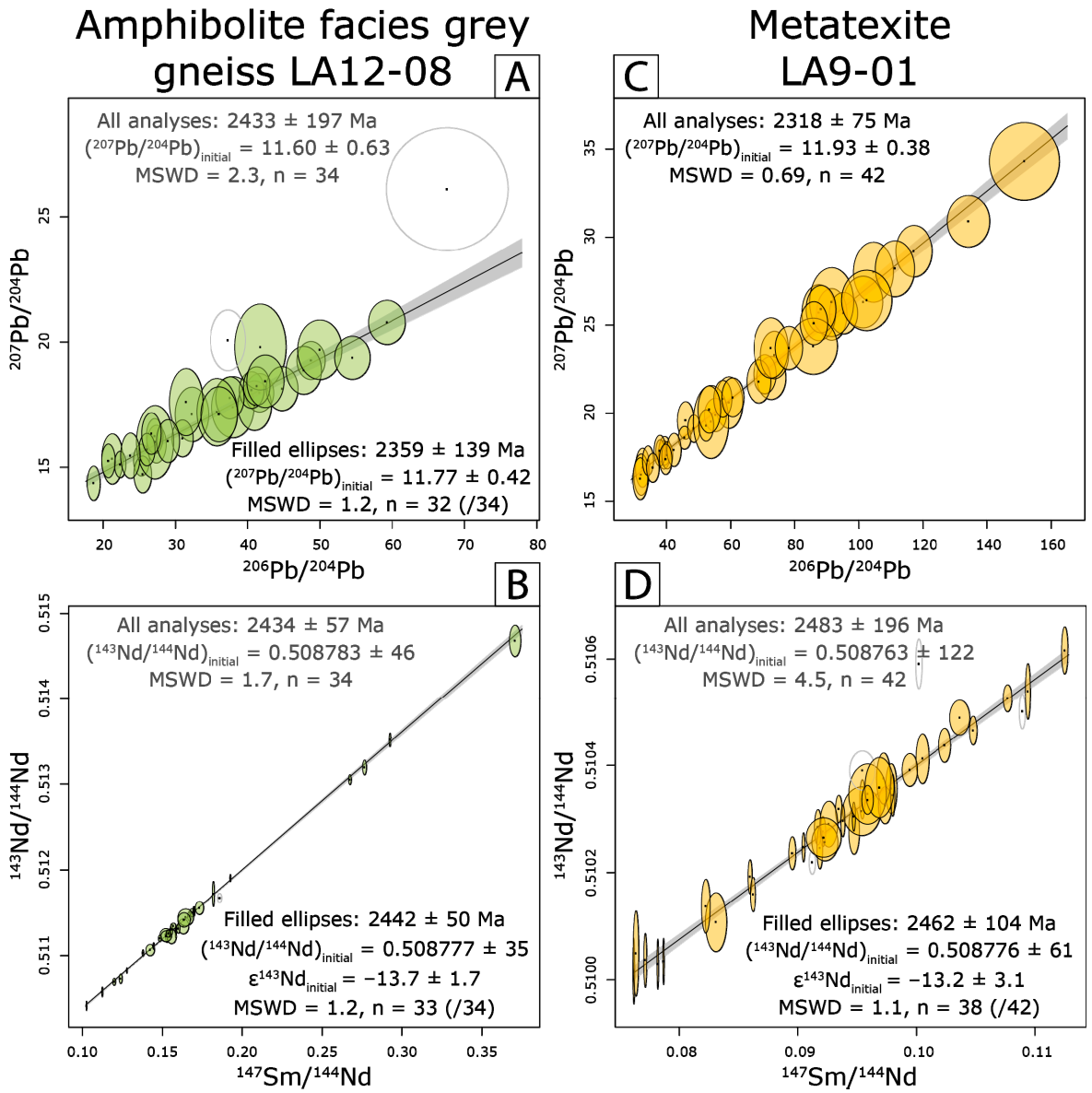

Figure 3. Results of the apatite U–Pb/Sm–Nd LASS analyses conducted in this study. (**A**) Apatite Pb–Pb isochron diagram for amphibolite facies grey gneiss LA12-08. (**B**) Apatite Sm–Nd isochron diagram for the amphibolite facies grey gneiss LA12-08. (**C**) Apatite Pb–Pb isochron diagram for the metatexite LA9-01. (**D**) Apatite Sm–Nd isochron diagram for the metatexite LA9-01. Uncertainty ellipses are shown at 95% confidence level. Uncertainty in apparent ages and in initial (Pb and Nd) ratios are reported at 95% confidence level. External uncertainties have been propagated in final ages and ratios. All diagrams plotted with IsoplotR-version 1001/639 [55]. Initial epsilon (ε) deviations are calculated with Sm–Nd isochron apparent age following Model-1 algorithm of [57] and include uncertainty in apparent age, CHUR model and decay constant.

Table 2. Summary of zircon U–Pb/Hf/O and apatite U–Pb/Sm–Nd isotopes LASS analyses and whole-rock Sm–Nd isotopes analyses conducted on the amphibolite grey gneiss facies LA12-08 and the metatexite LA9-01. Zircon isotopes analyses are from [5]. [1]: the meaning of whole-rock Sm–Nd isotopes results is discussed in the text.

Geological Event and Age			Emplacement-*ca.* 3.86 Ga	M1 Metamorphism -*ca.* 3.6 Ga	M2 Metamorphism -*ca.* 2.75–2.7 Ga	M3 Metamorphism -*ca.* 2.5–2.4 Ga
Amph. facies grey gneiss LA12-08	Zircon	$\varepsilon^{176}Hf_{initial}$	$+1.6 \pm 1.8$	-2.2 ± 0.6	$-17 \rightarrow -10$	?
		$\delta^{18}O_{VSMOW}$	5.4‰ → 6.6‰	+6.3‰	+6.5‰	?
	Apatite	$\varepsilon^{143}Nd_{initial}$	?	?	?	-13.7 ± 1.7
	Whole-Rock	$\varepsilon^{143}Nd_{present}$	-45 ± 0.5 (n = 3, MSWD = 206) [1]			
Metatexite LA9-01	Zircon	$\varepsilon^{176}Hf_{initial}$	-0.3 ± 0.8	-1.1 ± 0.7	$-20 \rightarrow -11$	?
		$\delta^{18}O_{VSMOW}$	5.4‰ → 6.6‰	up to +9‰	+6.8‰	?
	Apatite	$\varepsilon^{143}Nd_{initial}$	?	?	?	-13.2 ± 3.1
	Whole-Rock	$\varepsilon^{143}Nd_{present}$	-52 ± 1.5 (n = 3, MSWD = 13) [1]			

4.1. Apatite U–Pb/Sm–Nd Isotopes LASS Analyses

4.1.1. Amphibolite Facies Grey Gneiss LA12-08

Apatite grains from the amphibolite facies grey gneiss LA12-08 are commonly ≥ 200 µm long and *ca.* 150 µm wide (Figure 2A). No BSE zoning has been observed. Features resembling exsolution features, brighter in BSE, are present in some grains. Although these domains show chemical compositions of apatite they were, where possible, avoided for LASS analysis. It should nonetheless be noted that the analysis of domains with exsolution revealed no discrepancy in either U–Th–Pb or Sm–Nd isotope ratios from domains free of exsolution. Apatite crystals from the two gneisses studies were are stubby and prismatic, with either pyramidal or relatively rounded termination (Figure 2).

Thirty-four U–Pb/Sm–Nd LASS analyses were conducted on apatite grains from the grey gneiss LA12-08. As Pb-loss was obvious on the Tera–Wasserburg diagram (not shown), the apparent age was calculated from MLE regression on a $^{207}Pb/^{204}Pb$ versus $^{206}Pb/^{204}Pb$ diagram (Figure 3A). MLE regression of all 34 analyses yielded an isochron apparent age of 2433 ± 197 Ma (MSWD = 2.3, n = 34). The MSWD value of this regression indicated over-dispersion. Rejecting the two ellipses furthest from the regression yielded a statistically valid MLE regression of 2358 ± 139 Ma and $(^{207}Pb/^{204}Pb)_{initial}$ = 11.77 ± 0.42 (MSWD = 1.2, n = 32). Both Pb–Pb apparent ages were within uncertainty.

The 34 Sm–Nd single-spot isotope measurements, produced on the exact same ablation volume as the U–Pb isotope measurements, yielded an MLE regression apparent age of 2434 ± 57 Ma and a $(^{143}Nd/^{144}Nd)_{initial}$ of 0.508783 ± 0.000046 (MSWD = 1.7, n = 34, Figure 3B). This $(^{143}Nd/^{144}Nd)_{initial}$ value corresponded to $\varepsilon^{143}Nd_{initial} = -13.8 \pm 1.71 \,|\, 1.96$ at 2434 ± 57 Ma. Rejecting the ellipse furthest from the MLE regression yielded a statistically satisfying MLE regression featuring an apparent age of 2442 ± 50 Ma and a $(^{143}Nd/^{144}Nd)_{initial}$ of 0.508777 ± 0.000035 (MSWD = 1.2, n = 33, Figure 3B). This $(^{143}Nd/^{144}Nd)_{initial}$ value corresponded to $\varepsilon^{143}Nd_{initial} = -13.7 \pm 1.5 \,|\, 1.7$ deviation at 2442 ± 50 Ma. Both MLE regressions gave apparent ages and initial Nd ratios overlapping within uncertainty.

4.1.2. Metatexite LA9-01

Apatite grains from the metatexite LA9-01 showed similarities with those extracted from the amphibolite facies grey gneiss LA12-08: they were commonly ≥200 µm long and *ca.* 150 µm wide (Figure 2B). No BSE zoning was observed, and features resembling exsolution were present.

Forty-two U–Pb/Sm–Nd LASS analyses were conducted on apatite grains from the metatexite LA9-01. The MLE regression of the 42 U–Pb analyses yielded an apparent age of 2318 ± 75 Ma and $(^{207}Pb/^{204}Pb)_{initial}$ = 11.93 ± 0.38 (MSWD = 0.7) on a $^{207}Pb/^{204}Pb$ versus $^{206}Pb/^{204}Pb$ diagram Figure 3C). This apparent age overlapped with that obtained on the apatite from the amphibolite facies grey gneiss LA12-08.

The MLE regression of the 42 Sm–Nd isotope analyses produced on the same ablation volume as the U–Pb measurements yielded an Sm–Nd apparent age of 2483 ± 196 Ma and an initial Nd ratio of 0.508763 ± 0.000122 (Figure 3D). This MLE regression showed a MSWD value of 4.5, outside the acceptable range at 95% confidence. Rejecting the four analyses furthest from the regression yielded a statistically acceptable regression with an Sm–Nd apparent age of 2462 ± 104 Ma and an initial Nd ratio of 0.508776 ± 0.000061 (Figure 3D). Both Sm–Nd apparent ages and initial Nd ratios overlapped within uncertainty. The corresponding $\varepsilon^{143}Nd_{initial}$ deviation was equal to −13.2 ± 2.9 | 3.1. This $\varepsilon^{143}Nd_{initial}$ deviation overlapped with the value obtained on apatite from the amphibolite facies grey gneiss LA12-08.

4.2. Whole-Rock Sm–Nd Isotopes Analyses

Both samples were replicated three times to evaluate the effect of the possible incomplete dissolution of refractory phases.

The three replicate whole rock measurements of the amphibolite facies grey gneiss LA12-08 yielded $^{147}Sm/^{144}Nd$ and $^{143}Nd/^{144}Nd$ values that did not overlap (Figure 4A). The $^{147}Sm/^{144}Nd$ value ranged from 0.0939 to 0.1421, whereas $^{143}Nd/^{144}Nd$ ranged from 0.510271 ± 9 to 0.510473 ± 11. Differences in the Sm–Nd isotope compositions between the three replicates could be explained by either inhomogeneous rock powder or incomplete dissolution of refractory phases hosting Sm and Nd. It ought to be stressed at this point that the discrepancies in the Sm–Nd isotope ratios obtained over the three replicates, for both rocks, was likely not the result of the chemical protocol, as demonstrated by the analyses of secondary standard BHVO-2 which give precise (0.14ε precision, 2σ) and accurate ratios that overlapped with each other and overlapped with the accepted value. Regardless of the reason for the inconsistency obtained on the three replicates of both whole-rock analyses, this result shows the difficulty in interpreting the whole-rock isotopic data of rocks that have experienced multi-stage history.

The three replicates of the metatexite LA9-01 yield $^{147}Sm/^{144}Nd$ and $^{143}Nd/^{144}Nd$ were much closer than the results obtained on the amphibolite facies grey gneiss LA12-08. The $^{147}Sm/^{144}Nd$ value obtained on metatexite LA9-01 ranged from 0.0698 to 0.0709, whereas the $^{143}Nd/^{144}Nd$ value ranged from 0.509953 ± 12 to 0.510018 ± 17 (Figure 4A).

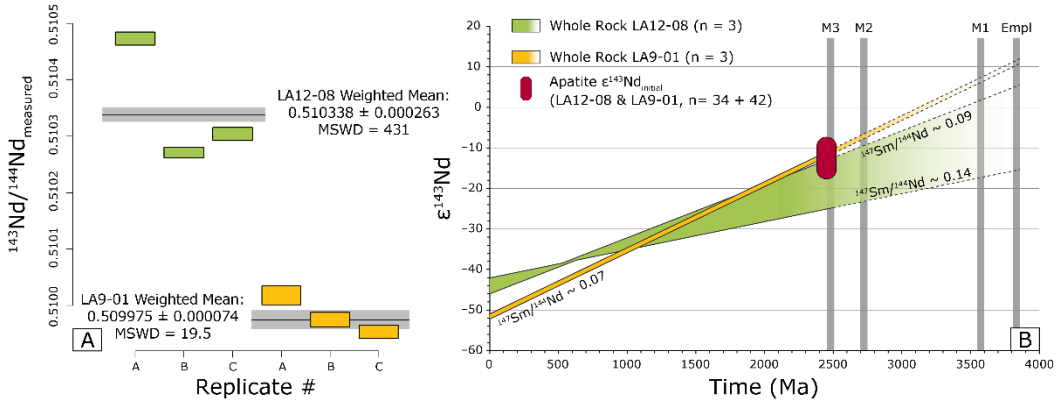

Figure 4. (**A**) Weighted mean diagram showing the measured $^{143}Nd/^{144}Nd$ whole-rock values for the three replicates (A, B and C) of the amphibolite facies grey gneiss LA12-08 and metatexite LA9-01. Diagram built with IsplotR [55]. (**B**) Evolution of the $\varepsilon^{143}Nd$ values back in the past. Empl.: Emplacement of the igneous protolith.

5. Discussions

5.1. Significance of Apatite U–Pb/Sm–Nd LASS Analyses

5.1.1. Effect of Metamorphism on U–Pb and Sm–Nd Isotope Signatures in Apatite and Zircon

It is widely accepted that zircon can preserve isotopic signatures through high-temperature metamorphism, to granulite facies [58]. Apatite is not so resilient and is relatively more reactive than zircon during metamorphic events [9], even below its diffusion closure temperature [59]. Our new results, and the U–Pb/Hf isotope analyses produced on zircon from the same hand-specimens studied here [5,47], were interpreted in the framework of the relative reactivity and the diffusion closure temperatures of apatite and zircon. Laboratory-controlled experiments have demonstrated that, for Pb and REE, diffusion rates are much higher in apatite crystals than zircon [60,61], indicating that, if considering diffusion only, zircon is more likely than apatite to preserve zoning and primary chemical/isotopic signatures.

5.1.2. Timing and Conditions of Apatite Crystallization in the Saglek Block

U–Pb and Sm–Nd isotope analyses of both populations of apatite presented here indicated crystallization in the early Paleoproterozoic, well after the protolith formation age (Figure 3). It is worth noting that Pb–Pb MLE regression reflects a dual-decay system (^{238}U–^{206}Pb and ^{235}U–^{207}Pb) and that Pb-diffusion would not affect the slope of MLE regression in the ^{207}Pb/^{204}Pb versus ^{206}Pb/^{204}Pb geometric space. Furthermore, this type of diagram has been successfully used in previous studies dealing with Archean REE-rich minerals (e.g., [27]). The statistically valid Pb–Pb isochron apparent ages presented in Figure 3A–C, coupled with clear BSE micro-structures (Figure 2), are interpreted as robust estimates of the final stages of Pb diffusion in these apatite crystals. The *ca.* 2.36–2.32 Ga Pb–Pb apparent ages obtained (Figure 3A–C) might mark the time where the rocks cooled below *ca.* 550 °C, the lower limit for Pb diffusion in apatite [61]. The apatite Sm–Nd isochron ages obtained here were slightly older than the Pb–Pb apparent ages (Figure 3 and Table 1), although virtually within uncertainty. Experiments of REE diffusion in apatite indicated diffusion rates that were slower by about two orders of magnitude for REE compared with Pb, irrespective of temperature [60]. It is thus not surprising that we observed Sm–Nd apparent ages that were older than the Pb–Pb apparent ages in apatite. The lower limit of apatite REE diffusion is around 670 °C [60], so the Sm–Nd apparent ages of *ca.* 2.45 Ga (Figure 3) might mark the time when apatite crystals, and their host rock, cooled below the 670 °C isotherm. Detailed geochronological and metamorphic studies of the meta-sedimentary rocks exposed in the Saglek Block would be needed to provide more precise and more definite pressure–temperature constraints. Regardless, the two time–temperature estimates obtained from our results yielded a minimum cooling rate of 1.3 °C/Ma, a value consistent with that obtained by [34] for the Saglek block, using a similar approach.

Since the Sm–Nd apparent ages of both apatite populations overlapped, and were broadly coincident with the Pb–Pb apparent ages, we calculated a weighted average with the four isochron apparent ages (two Pb–Pb isochron apparent ages + two Sm–Nd isochron apparent ages). These four isochron apparent ages yielded a weighted mean of 2408 ± 104 Ma (95% confidence level including overdispersion, MSWD = 3.1). The MSWD value of 3.1 implied that these four isochron apparent ages had only a *ca.* 2.5% chance of representing a single homogeneous population, so this weighted mean ought to be viewed only as an approximation of the apatite crystallization age.

Lastly, no xenocryst core was observed in any of the two apatite populations investigated here, despite the relatively large number of grains imaged and analyzed on each population (34 and 42 analyses). This observation can be interpreted two ways. Either temperatures were largely above apatite Pb- and REE-closure temperatures during the *ca.* 2.5–2.4 Ga event in the Saglek Block, i.e., above 700 °C [60], and these crystals precipitated in a melt-rich environment, or the apatite populations were produced by a process of complete dissolution–reprecipitation at temperatures << 700 °C [62]. The latter process has mostly been documented in zircon [58]. However, apatite dissolution–reprecipitation would likely result in newly formed apatite crystals with numerous inclusions [63,64], a feature not observed in any of our two populations. Despite this observation and the evidence of magmatic activity at *ca.* 2.5–2.4 Ga in the Saglek Block [40,65], that would favor—at least locally—the presence of a melt-dominated environment as the crystallization medium for these apatite populations, no zircon domains showing *ca.* 2.5–2.4 Ga U–Pb ages were reported in any of the zircon grains extracted from these two rocks. Thus, either the two populations of apatite crystallized at *ca.* 2.5–2.4 Ga in a melt-rich environment that did not have the ability to dissolve zircon, or the apatite crystallization took place in a melt-free environment. The pressure–temperature metamorphic history of the Saglek Block is presently too limited to clearly define which of the two processes/conditions dominated.

5.1.3. Correlation with Regional Events

The regional isotopic ages obtained on zircon and REE-rich minerals are presented in Figures 3 and 5. The weighted average age of *ca.* 2.4 Ga calculated from the apatite U–Pb/Sm–Nd LASS analyses conducted here was *ca.* 200 Ma older than the U–Pb apparent age measured on apatite crystals from two meta-igneous felsic rocks sampled on Nulliak Island, and on the shore of Tigigakyuk Inlet *ca.* 2.18 Ga and *ca.* 2.26 Ga, respectively (see [39]). The apatite crystals from the Saglek block investigated by [28], sample UV-1-BR, showed U–Pb apparent ages of *ca.* 2.73 Ga, whereas the Sm–Nd isochron apparent age was *ca.* 2.43 ± 0.13 Ga, i.e., *ca.* 300 Myr younger. A similar observation can be made for the U–Pb/Sm–Nd LASS analyses of monazite crystals from the same rock. Monazite U–Pb apparent ages ranged from *ca.* 2790 to *ca.* 2480, whereas the Sm–Nd isochron obtained on the same crystal volume yielded an apparent age of 3253 ± 192 Ma (Table 3). The difference observed between the monazite U–Pb and Sm–Nd apparent ages was not discussed in [28]; however, it could be analogous to the mixing process observed in titanite crystals extracted from a metasediment sampled on the Nulliak Island [30].

Table 3. U–Pb and Sm–Nd isotopes date of REE-rich minerals from the Saglek Block and of co-hosted zircon. LASS: laser ablation split stream; LA–ICP–MS: laser ablation inductively coupled plasma mass spectrometer. T–W: Tera–Wasserburg diagram. U.I.: Wetherill upper intercept discordia. Dates noted * are recalculated to obtain statistically robust isochron fits and include systematic uncertainties. Ø: not known. [A]: the metatexite LA9-01 is considered coeval with the amphibolite facies grey gneiss LA12-08. [B]: the meaning of this monazite date is discussed in Section 5.1.3.

Sample ID	Mineral Analyzed	Method	Age Calculation	Date (Ma) ± Uncertainty (95%)	Zircon Age (Ma)	Reference
74−161 A	Apatite	Dissolution	$^{207}Pb/^{206}Pb$	2384	2825	[43]
74−161 B	Apatite	Dissolution	$^{207}Pb/^{206}Pb$	2385	Ø	[43]
74−161 C	Apatite	Dissolution	$^{207}Pb/^{206}Pb$	2388	3044	[43]
74–40 A	Apatite	Dissolution	$^{207}Pb/^{206}Pb$	2491	3334	[43]
74−161 F	Apatite	Dissolution	$^{207}Pb/^{206}Pb$	2391	3485	[43]

Table 3. *Cont.*

Sample ID	Mineral Analyzed	Method	Age Calculation	Date (Ma) ± Uncertainty (95%)	Zircon Age (Ma)	Reference
L1429	Apatite	LA-ICP-MS	$^{207}Pb/^{206}Pb$	2182 ± 27	2710 ± 14	[39]
L1439	Apatite	LA-ICP-MS	$^{207}Pb/^{206}Pb$	2260 ± 38	Ø	[39]
UV-1-BR	Apatite	LASS	U.I.	2734 ± 31	3654 ± 23	[28]
			Sm–Nd isochron	2459 ± 89 *		
LA12-08	Apatite	LASS	Pb–Pb isochron	2359 ± 139	3860 ± 10	This study
			Sm–Nd isochron	2442 ± 50		
LA9-01	Apatite	LASS	Pb–Pb isochron	2318 ± 75	3860 ± 10 [A]	This study
			Sm–Nd isochron	2462 ± 104		
75–285 C	Titanite	Dissolution	$^{207}Pb/^{206}Pb$	2516	Ø	[43]
75–271 E	Titanite	Dissolution	$^{207}Pb/^{206}Pb$	2491	Ø	[43]
75–271 D	Titanite	Dissolution	$^{207}Pb/^{206}Pb$	2508	Ø	[43]
74−161 D	Titanite	Dissolution	$^{207}Pb/^{206}Pb$	2514	Ø	[43]
75–262	Titanite	Dissolution	$^{207}Pb/^{206}Pb$	2492	*ca.* 2505	[43]
LA13−19	Titanite	LASS	T–W Intercept	2529 ± 15	≥ 3500	[30]
L1419	Monazite	EPMA	Deconvoluted	2660 ± 22 and 2515 ± 41	3635 ± 42	[39]
L1415	Monazite	EPMA	Deconvoluted	2615 ± 19 and 2540 ± 18	3725 ± 33	[39]
L1439	Monazite	EPMA	Deconvoluted	2718 ± 33 and 2463 ± 31	Ø	[39]
L1450	Monazite	EPMA	Mean	2676 ± 15	Ø	[39]
L1487	Monazite	EPMA	Mean	2724 ± 26	Ø	[39]
UV-1-BR	Monazite	LASS	Range	*ca.* 2790 to 2480	3654 ± 23	[28]
			Sm–Nd isochron	3253 ± 192 *,[B]		
L1487	Monazite	SIMS	Mean	2709 ± 14	2742 ± 8	[40]
L1492	Monazite	SIMS	Mean	2727 ± 6	*ca.* 3280 (max)	[40]
L1458	Monazite	SIMS	Mean	2551 ± 6 and 2522 ± 8	Ø	[40]

Taken at face value, the U–Pb and Sm–Nd apparent ages seem to indicate apatite crystallization, or at least diffusion closure, separated by *ca.* 600 Myr (Figure 5). However, it remains surprising that apatite crystals hosted in rocks separated by ~10 km display such different Sm–Nd isotopic apparent ages: *ca.* 2.18 Ga [39] through *ca.* 2.3–2.4 Ga (this study, Figure 3), and up to *ca.* 2.73 Ga [28]. We consider it unlikely that such geographically proximal samples, part of the same rock package, with no evidence of a major tectonic break or lineament between them, can experience the significantly different pressure–temperature histories required to explain the spectrum of ages in Figure 5. Consequently, based on the presently available dataset, we attribute the *ca.* 2.2 Ga apatite apparent ages to recrystallization of apatite crystals in the presence of locally derived fluids (i.e., 10 s to 100 s of meters), instead of any single regional thermal event. The *ca.* 2.5–2.4 Ga metamorphic event in the Saglek block has been interpreted as a high grade metamorphic event—accompanied by localized partial melting, as testified by granitoid bodies with *ca.* 2.55 Ga intrusion ages meta-monzonite L1412 [40]—possibly related to collision between the Saglek Block and Hopedale Block [39,66]. The *ca.* 2.4 Ga age recorded by U–Pb and

Sm–Nd systems in the apatite grains that we have studied is seen here as part of the waning stages of the *ca.* 2.5–2.4 Ga thermal event [39]. The range of apatite U–Pb/Sm–Nd isochron ages we found also overlap both the EPMA monazite U–Pb ages reported in [39] and the LA–ICP–MS monazite U–Pb ages reported in [28] (see Figure 5). The ability of REE-rich minerals, and particularly apatite, to react/recrystallize under relatively low-T metamorphic conditions, down to greenschist facies, means that accurately dating the end of the *ca.* 2.5–2.4 Ga Saglek metamorphic event remains difficult.

Lastly, our results also suggest that the samples studied here either remained at mid-amphibolite facies conditions between 2.7 and 2.5 Ga, or were exhumed into the upper crust after 2.7 Ga, and then reburied to amphibolite facies conditions at 2.5 Ga. In either case, the *ca.* 2.7 Ga zircon metamorphic ages documented in the Saglek Block cannot be considered as marking the termination of regional metamorphic events. Instead, elemental (including REE) and isotopic redistribution occurred at the crystal scale after the latest zircon crystallization event. Our results undoubtedly indicate that, in the metamorphic systems studied here, the most recent redistribution of Hf isotopes occurred *ca.* 200 Ma, before the most recent redistribution of Sm and Nd isotopes. These two isotopes systems thus do not reflect the same events. A similar observation can be made at the terrane scale: crystallization ages obtained on REE-rich minerals in the Saglek Block were not consistent with, and were systematically younger than, the vast majority of zircon U–Pb crystallization ages obtained on zircon from the same hand-specimen (Figure 5). Hence, there is a diachronous redistribution of Hf and Nd isotopes at both the terrane scale and the hand-specimen scale.

5.2. Diachronous Redistribution of Hf and Nd Isotopes in the Saglek Block

The zircon U–Pb/Hf and REE-rich minerals U–Pb/Sm–Nd isotope results obtained from the felsic igneous rocks from the Mt. Edgar Complex (Pilbara craton, Australia) showed that these phases can be coeval [67]. In this example, zircon, monazite, titanite and apatite from a Pilbara basement rock showed Paleoarchean ages and chondritic Hf and Nd initial compositions, i.e., indicative of no significantly depleted source mantle and no Hf–Nd decoupling at that time, in this area. Yet, in most ancient, preserved rocks, zircon and REE-rich minerals are not coeval, and zircon usually pre-dates REE-rich minerals, which are typically of metamorphic origin. In this case, REE-rich minerals can be used to constrain the nature of the fluids involved during metamorphism. Our results for the Saglek Block basement rocks fall into this latter category.

Apatite crystals investigated in this study have been extracted from two meta-igneous rocks containing zircon previously characterized for U–Pb/Hf/O isotopes (Figures 6 and 7).

The oldest zircon domains retrieved from these two gneisses yielded *ca.* 3.86 Ga U–Pb crystallization age, i.e., *ca.* 1.5 Gyr older than the Pb–Pb and Sm–Nd ages obtained on apatite crystals from the same rocks. Furthermore, the apatite crystals studied here were interpreted as being formed during the *ca.* 2.5–2.4 Ga metamorphic event identified in the Saglek Block by previous studies (see Section 5.1), whereas the oldest zircon domains have been interpreted as reflecting crystallization of the *primary* magma [5]. Thus, the Sm–Nd isotope compositions of these apatite grains cannot confidently be regarded as reflecting the composition of the primary magma from which the oldest zircon domains precipitated at *ca.* 3.86 Ga ago, because of the strong possibility of Nd mobility during metamorphism (e.g., [19,27,28,30]). If the length-scale of Nd mobility during metamorphism was beyond that of a hand-specimen (~20 cm), then the measured whole-rock Sm–Nd isotope compositions cannot confidently be regarded as reflecting the composition of the primary magma. Such *large-scale* Nd mobility can be envisioned in the rocks of the Saglek Block, in light of the fact that the whole-rock Nd isotopic compositions do not lie perfectly on the Sm–Nd isochron drawn from apatite Sm–Nd compositions. In other words, these two populations of apatite are out of equilibrium with their host rocks. Thus, this could suggest an open system behavior of Nd isotopes during the *ca.* 2.5–2.4 Ga events in the Saglek Block. See also [28] for open-system bahviour of Nd during the 2.7 Ga metamorphic event.

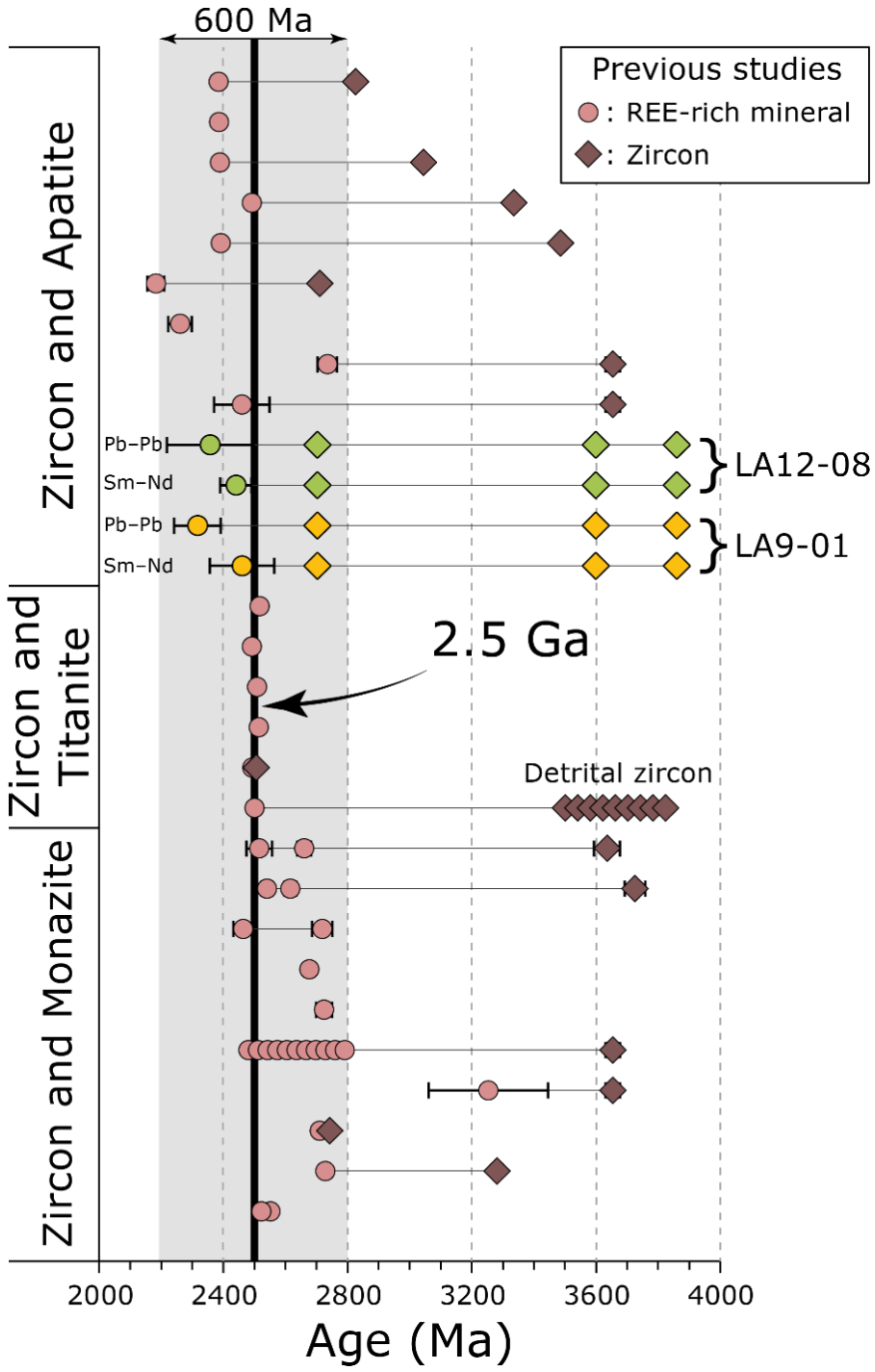

Figure 5. Compilation of REE-rich mineral ages from the Saglek Block and corresponding zircon age obtained on the same rock hand-specimen. Diamond symbols are zircon analyses, circle symbols are either apatite or titanite or monazite analyses. Each line represents one hand-specimen. Uncertainties are reported at 95% confidence interval. Data from: [5,28,30,39,40,43,47] and this study. Details about the distribution of ages and Hf–Nd isotopes signatures are shown in Figure 6.

In-situ investigations of Hf isotopic compositions in the Saglek Block have clearly identified the redistribution of Hf isotopes [5,46,47] via: (i) dissolution–reprecipitation of zircon during a *ca.* 3.6 Ga metamorphic event, with newly formed zircon crystals/domains inheriting Hf from the older, dissolved zircon domains; and (ii) dissolution–reprecipitation of zircon during a *ca.* 2.7 Ga metamorphic event with clear evidence of input of a radiogenic Hf. See Figures 6 and 7 for likely exotic origin.

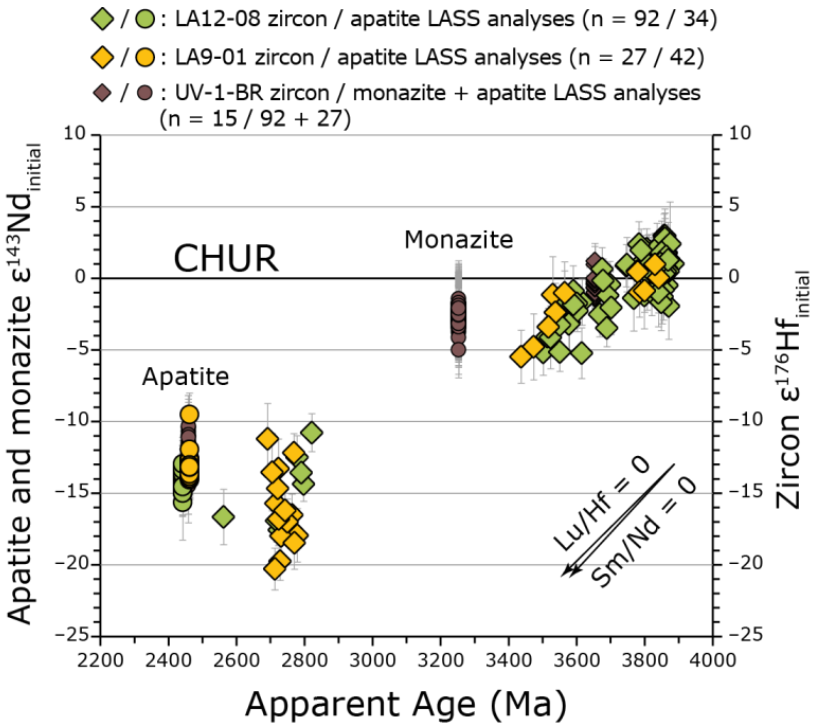

Figure 6. Epsilon (ε) ^{143}Nd and ^{176}Hf versus apparent age (Ma) relations for zircon and apatite from the same rock compared with monazite and apatite from a nearby rock. Diamond symbols are zircon analyses, circles are either apatite (for samples LA12-08, LA9-01 and UV-1-BR) or monazite analyses (UV-1-BR only). Zircon apparent ages are ^{207}Pb/^{206}Pb apparent ages for LA12-08 and LA9-01 and upper intercept Discordia age for UV-1-BR. Apatite and monazite apparent ages are those calculated from the Sm–Nd isochron array (Figure 3). Uncertainty bars are reported at 95% confidence level. Zircon LASS analyses for LA12-08 and LA9-01 are from [5,47]. UV-1-BR LASS analyses are from [28].

Redistribution of both Hf-isotopes and Sm–Nd isotopes is, in Saglek Block examples presented above, clearly a consequence of phase equilibrium stability of the main hosts for these two isotope systems. In the felsic metamorphic rocks studied, zircon is overall less prone than apatite, titanite and monazite to breakdown/reaction during metamorphism; thus, there is a higher chance of preserving the Hf-compositions of the primary magma in zircon core domains. In contrast, the common tendency of REE-rich phases to re-crystallize during high-grade metamorphism means that the accurate preservation of magmatic Sm–Nd isotopic compositions is less likely.

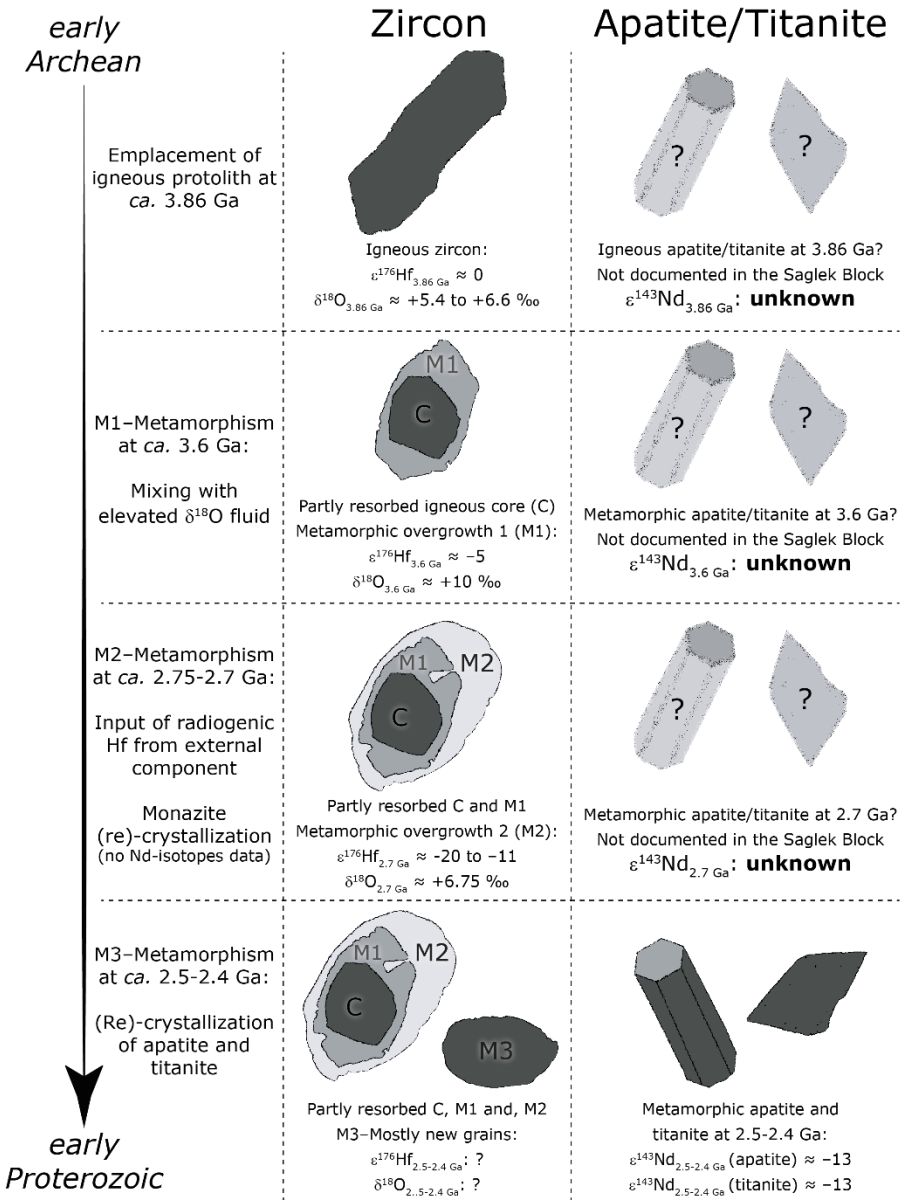

Figure 7. Evolution of Hf- and Nd-isotopes compositions of zircon and REE-rich minerals throughout the metamorphic history of the Archean Saglek Block.

5.3. The Neoarchean Metamorphic History of the Saglek Block

Although a definitive history of the duration of the Neoarchean metamorphic event (s ?) in the Saglek Block is still pending, numerous studies have reported late Neoarchean U–Pb ages measured in accessory phases, such as zircon, titanite and apatite [5,28,30,38–40,43,46,47,68]. Based on these studies, and the results presented here, two thermal events seem to have occurred during the Neoarchean/early-Paleoproterozoic: one at *ca.* 2.7 Ga, largely recorded in metamorphic zircon growth, and a younger event at *ca.* 2.5–2.4 Ga, largely observed in REE-rich accessories. Thus far, no Sm–Nd isotopic compositions of *ca.* 2.7 Ga-old REE-rich accessories have been reported, precluding any comparison between zircon Hf- and apatite/monazite/titanite Nd-isotopic compositions during this event. This might be because the later ~2.5 Ga event eradicated most evidence of the 2.7 event in REE-rich minerals. Nevertheless, Hf-isotopic compositions of the *ca.* 2.7 Ga zircon domains clearly indicate the reworking of crustal material with strongly sub-chondritic Hf isotope signatures, i.e., ε^{176}Hf ~ −20 to −11 (Figure 7). This late zircon growth event also provides

clear evidence of mixing between crustal Hf and a much more radiogenic Hf component in some metamorphic zircon populations [47].

In addition to the results presented here (Figure 3), two recent studies also show old inherited crustal Nd isotopic signatures in *ca.* 2.5 Ga REE-rich accessories, with $\varepsilon^{143}Nd < -10$ [28,30]. These data are consistent with the evidence offered by Hf isotopic compositions in *ca.* 2.7 Ga zircon domains. However, the overall picture is made more complex when considering the likely involvement of fluid-carrying radiogenic Nd that was involved in the crystallization of titanite at *ca.* 2.5 Ga [30]. The involvement of exotic components in the late Archean metamorphism of the Saglek Block was suggested early in the history of study of these rocks, based on pioneering in-situ zircon Pb isotopes analyses [22].

In summary, the two Neoarchean/early-Paleoproterozoic metamorphic events of the Saglek Block seem to involve the reworking of local crustal lithologies, both igneous and sedimentary, with the subtle but unequivocal indications of exotic fluids carrying Hf and Nd with isotopic compositions more radiogenic than the regional crustal signature. Based on the presently available datasets [5,24,38–40,46,47,68], the igneous and metamorphic history of the Saglek Block can be summarized as followed:

1. Igneous activity at *ca.* 3.87 Ga was sourced from a mantle domain that had experienced only subtle prior fractionation of parent–daughter isotopes, which had incorporated hydrothermally altered material before partial melting. This is based on previously published zircon U–Pb/Hf/O-isotopes analyses [5,47];
2. High-grade metamorphism at *ca.* 3.5 Ga. This event caused the partial re-opening of older zircon domains (major Pb-loss) making it difficult to identify the *true* emplacement age of older igneous rocks. New zircon growth was also recognized during this event. Zircon Hf-isotopes largely indicate intra-crustal reworking, whereas zircon O–isotopes revealed the involvement of mature supracrustal precursors (mafic volcanics ± clastic/chemical sediments);
3. An early-Neoarchean regional high-grade metamorphism at *ca.* 2.7 Ga, that also caused the partial re-opening of zircon and significant Pb-loss. New zircon growth has also been identified during this event. Several populations of REE-rich phases also yielded a *ca.* 2.7 Ga-old U–Pb apparent age;
4. Late-Neoarchean/early-Paleoproterozoic metamorphism at *ca.* 2.5–2.4 Ga (+2.2 Ga?). Massive (re)-recrystallization of REE-rich mineral phases at the regional scale, especially apatite and titanite. Sm–Nd isotopes indicated intra-crustal reworking. An accurate dating of the termination of this event cannot yet be constrained, due to the readiness of REE-rich phases to react under low-grade metamorphism in fluid-present environments.

6. Conclusions

A combination of zircon U–Pb/Hf and apatite U–Pb/Sm–Nd isotope compositions can illuminate the protracted metamorphic history of ancient crustal terranes. These two approaches were used here to show the diachronous redistribution of Hf and Nd isotopes at the hand-specimen scale in the Saglek Block—a terrane formed at circa 3.87 Ga. We showed a time lag of 200 Myr between the youngest zircon overgrowths, the host for Hf, and the crystallization of most apatite, the host for Nd. Consequently, in these rocks, Hf and Nd isotopic signatures do not reflect contemporaneous geological events. The decoupling of these isotope systems and the precarious use of whole rock isotope measurements is thus clear. The new in-situ Nd-isotope data presented here reveal that intra-crustal reworking was a major process during the *ca.* 2.5–2.4 Ga-old regional metamorphic event that shaped the later evolution of the Saglek Block. Nonetheless, this effect should not mask the role played by external fluids, derived from juvenile material, that could have been locally involved in the two Neoarchean/early-Paleoproterozoic metamorphic events recognized in the Saglek Block.

Supplementary Materials: The following are available online at https://www.mdpi.com/article/10.3390/geosciences12010036/s1, Table S1: WR and in-situ U-Pb and Sm-Nd isotope analyses.

Author Contributions: Conceptualization, A.V., E.T. and D.G.P.; methodology, A.V., Y.L. and C.S.; validation, A.V., Y.L. and C.S.; writing—original draft preparation, A.V. and E.T. writing—review and editing, Y.L., C.S. and D.G.P.; funding acquisition, D.G.P. All authors have read and agreed to the published version of the manuscript.

Funding: This research was funded by Natural Sciences and Engineering Research Council of Canada Discovery Grants Program and the Canada First Research Excellence Fund: Metal Earth Project to D.G.P. The field campaign was funded by the Agence Nationale de la Recherche to E.T. (ANR-11-JS56–0012).

Institutional Review Board Statement: Not applicable.

Informed Consent Statement: Not applicable.

Data Availability Statement: The data presented in this study are available in supplementary material.

Acknowledgments: The authors are grateful to two anonymous reviewers for their constructive comments on this manuscript. This is Metal Earth contribution MERC-ME-2022-01. This work has been part-supported by a grant from the European Research Council (ERC) under the European Union's Horizon H2020 research and innovation program (Synergy Grant MEET, grant agreement no. 856555). Sebastien Roubinet and Anne-Lise Vacher-Morazzani are warmly thanked for assistance in the field and unrivalled seamanship in the Labrador Sea.

Conflicts of Interest: The authors declare no conflict of interest.

References

1. Hiess, J.; Bennett, V.C.; Nutman, A.P.; Williams, I.S. In situ U–Pb, O and Hf isotopic compositions of zircon and olivine from Eoarchaean rocks, West Greenland: New insights to making old crust. *Geochim. Cosmochim. Acta* **2009**, *73*, 4489–4516. [CrossRef]
2. Hiess, J.; Bennett, V.C.; Nutman, A.P.; Williams, I.S. Archaean fluid-assisted crustal cannibalism recorded by low $\delta^{18}O$ and negative $\varepsilon_{Hf(T)}$ isotopic signatures of West Greenland granite zircon. *Contrib. Mineral. Petrol.* **2011**, *161*, 1027–1050. [CrossRef]
3. Hiess, J.; Bennett, V.C. Chondritic Lu/Hf in the early crust–mantle system as recorded by zircon populations from the oldest Eoarchean rocks of Yilgarn Craton, West Australia and Enderby Land, Antarctica. *Chem. Geol.* **2016**, *427*, 125–143. [CrossRef]
4. Petersson, A.; Kemp, A.I.; Hickman, A.H.; Whitehouse, M.J.; Martin, L.; Gray, C.M. A new 3.59 Ga magmatic suite and a chondritic source to the east Pilbara Craton. *Chem. Geol.* **2019**, *511*, 51–70. [CrossRef]
5. Vezinet, A.; Pearson, D.G.; Thomassot, E.; Stern, R.A.; Sarkar, C.; Luo, Y.; Fisher, C.M. Hydrothermally-altered mafic crust as source for early Earth TTG: Pb/Hf/O isotope and trace element evidence in zircon derived from TTG of the Eoarchean Saglek Block, N. Labrador. *EPSL* **2018**, *503*, 95–107. [CrossRef]
6. Dhuime, B.; Hawkesworth, C.J.; Delavault, H.; Cawood, P.A. Rates of generation and destruction of the continental crust: Implications for continental growth. *Philos. Trans. R. Soc. A Math. Phys. Eng. Sci.* **2018**, *376*, 20170403. [CrossRef]
7. Korenaga, J. Estimating the formation age distribution of continental crust by unmixing zircon ages. *EPSL* **2018**, *482*, 388–395. [CrossRef]
8. Korenaga, J. Hadean geodynamics and the nature of early continental crust. *Precambr. Res.* **2021**, *359*, 106178. [CrossRef]
9. Engi, M. Petrochronology based on REE-minerals: Monazite, allanite, xenotime, apatite. *Rev. Mineral. Geochem.* **2017**, *83*, 365–418. [CrossRef]
10. Bruand, E.; Fowler, M.; Storey, C.; Laurent, O.; Antoine, C.; Guitreau, M.; Heilimo, E.; Nebel, O. Accessory mineral constraints on crustal evolution: Elemental fingerprints for magma discrimination. *Geochem. Perspect. Letters* **2020**, *13*, 7–12. [CrossRef]
11. Aleinikoff, J.N.; Wintsch, R.P.; Fanning, C.M.; Dorais, M.J. U–Pb geochronology of zircon and polygenetic titanite from the Glastonbury Complex, Connecticut, USA: An integrated SEM, EMPA, TIMS, and SHRIMP study. *Chem. Geol.* **2002**, *188*, 125–147. [CrossRef]
12. Foster, G.L.; Vance, D. In situ Nd isotopic analysis of geological materials by laser ablation MC-ICP-MS. *J. Anal. At. Spectrom.* **2006**, *21*, 288–296. [CrossRef]
13. Storey, C.D.; Jeffries, T.E.; Smith, M. Common lead-corrected laser ablation ICP–MS U–Pb systematics and geochronology of titanite. *Chem. Geol.* **2006**, *227*, 37–52. [CrossRef]
14. McFarlane, C.R.M.; McCulloch, M.T. Coupling of in-situ Sm–Nd systematics and U–Pb dating of monazite and allanite with applications to crustal evolution studies. *Chem. Geol.* **2007**, *245*, 45–60. [CrossRef]
15. Frost, B.R.; Chamberlain, K.R.; Schumacher, J.C. Sphene (titanite): Phase relations and role as a geochronometer. *Chem. Geol.* **2001**, *172*, 131–148. [CrossRef]
16. Kohn, M.J. Titanite petrochronology. *Rev. Mineral. Geochem.* **2017**, *83*, 419–441. [CrossRef]

17. Spear, F.S.; Pyle, J.M. Apatite, monazite, and xenotime in metamorphic rocks. *Rev. Mineral. Geochem.* **2002**, *48*, 293–335. [CrossRef]
18. Henrichs, I.A.; O'Sullivan, G.; Chew, D.M.; Mark, C.; Babechuk, M.G.; McKenna, C.; Emo, R. The trace element and U-Pb systematics of metamorphic apatite. *Chem. Geol.* **2018**, *483*, 218–238. [CrossRef]
19. Janots, E.; Austrheim, H.; Spandler, C.; Hammerli, J.; Trepmann, C.A.; Berndt, J.; Magnin, V.; Kemp, A.I. Rare earth elements and Sm-Nd isotope redistribution in apatite and accessory minerals in retrogressed lower crust material (Bergen Arcs, Norway). *Chem. Geol.* **2018**, *484*, 120–135. [CrossRef]
20. Taylor, R.J.; Kirkland, C.L.; Clark, C. Accessories after the facts: Constraining the timing, duration and conditions of high-temperature metamorphic processes. *Lithos* **2016**, *264*, 239–257. [CrossRef]
21. Bridgwater, D.; Rosing, M.; Schiøtte, L.; Austrheim, H. The effect of fluid-controlled element mobility during metamorphism on whole rock isotope systems, some theoretical aspects and possible examples. In *Fluid Movements—Element Transport and the Composition of the Deep Crust*; Springer: Dordrecht, The Netherlands, 1989; pp. 277–298.
22. Schiøtte, L. On the possible role of fluid transport in the distribution of U and Pb in an Archaean gneiss complex. In *Fluid Movements—Element Transport and the Composition of the Deep Crust*; Springer: Dordrecht, The Netherlands, 1989; pp. 299–317.
23. Moorbath, S.; Whitehouse, M.; Kamber, B. Extreme Nd-isotope heterogeneity in the early Archaean—fact or fiction? Case histories from northern Canada and West Greenland. *Chem. Geol.* **1997**, *135*, 213–231. [CrossRef]
24. Vezinet, A.; Pearson, D.G.; Thomassot, E. Effects of contamination on whole-rock isochrons in ancient rocks: A numerical modelling approach. *Lithos* **2021**, *386–387*, 106040. [CrossRef]
25. Hammerli, J.; Kemp, A.; Spandler, C. Neodymium isotope equilibration during crustal metamorphism revealed by in situ microanalysis of REE-rich accessory minerals. *EPSL* **2014**, *392*, 133–142. [CrossRef]
26. Gregory, C.J.; McFarlane, C.R.; Hermann, J.; Rubatto, D. Tracing the evolution of calc-alkaline magmas: In-situ Sm–Nd isotope studies of accessory minerals in the Bergell Igneous Complex, Italy. *Chem. Geol.* **2009**, *260*, 73–86. [CrossRef]
27. Hammerli, J.; Kemp, A.I.; Whitehouse, M.J. In situ trace element and Sm-Nd isotope analysis of accessory minerals in an Eoarchean tonalitic gneiss from Greenland: Implications for Hf and Nd isotope decoupling in Earth's ancient rocks. *Chem. Geol.* **2019**, *524*, 394–405. [CrossRef]
28. Fisher, C.M.; Bauer, A.M.; Luo, Y.; Sarkar, C.; Hanchar, J.M.; Vervoort, J.D.; Tapster, S.R.; Horstwood, M.; Pearson, D.G. Laser ablation split-stream analysis of the Sm-Nd and U-Pb isotope compositions of monazite, titanite, and apatite–Improvements, potential reference materials, and application to the Archean Saglek Block gneisses. *Chem. Geol.* **2020**, *539*, 119493. [CrossRef]
29. Zhou, G.; Fisher, C.M.; Luo, Y.; Pearson, D.G.; Li, L.; He, Y.; Wu, Y. A clearer view of crustal evolution: U-Pb, Sm-Nd, and Lu-Hf isotope systematics in five detrital minerals unravel the tectonothermal history of northern China. *Geol. Soc. Am. Bull.* **2020**. [CrossRef]
30. Vezinet, A.; Thomassot, E.; Pearson, D.G.; Luo, Y.; Sarkar, C.; Ternois, S. One mineral, two conflicting isotopic clocks: The effect of metamorphic mixing at the crystal scale. *G-cubed manuscript in preparation*.
31. Hurst, R.W.; Bridgwater, D.; Collerson, K.D.; Wetherill, G.W. 3600-My Rb-Sr ages from very early Archaean gneisses from Saglek Bay, Labrador. *EPSL* **1975**, *27*, 393–403. [CrossRef]
32. Bridgwater, D.; Collerson, K.D. The major petrological and geochemical characters of the 3,600 My Uivak gneisses from Labrador. *Contrib. Mineral. Petrol.* **1976**, *54*, 43–59. [CrossRef]
33. Collerson, K.D.; Bridgwater, D. Metamorphic development of early Archaean tonalitic and trondhjemitic gneisses: Saglek area, Labrador. In *Trondhjemites, Dacites and Related Rocks*; Barker, F., Ed.; Developments in Petrology; Elsevier: Amsterdam, The Netherlands, 1979; Volume 6, pp. 205–274.
34. Wendt, J.I.; Collerson, K.D. Early Archaean U/Pb fractionation and timing of late Archaean high-grade metamorphism in the Saglek–Hebron segment of the North Atlantic Craton. *Precambr. Res.* **1999**, *93*, 281–297. [CrossRef]
35. Schiøtte, L.; Bridgwater, D.; Collerson, K.D.; Nutman, A.P.; Ryan, B. Chemical and isotopic effects of late Archaean high-grade metamorphism and granite injection on early Archaean gneisses, Saglek-Hebron, northern Labrador. *Geol. Soc. Lond. Spec. Publ.* **1986**, *24*, 261–273. [CrossRef]
36. Barton, J.M.J. Rb-Sr isotopic characteristics and chemistry of the 3.6-by Hebron gneiss, Labrador. *EPSL* **1975**, *27*, 427–435. [CrossRef]
37. Collerson, K.D. The Archean gneiss complex of northern Labrador. 2. Mineral ages, secondary isochrons, and diffusion of strontium during polymetamorphism of the Uivak gneisses. *Can. J. Earth Sci.* **1983**, *20*, 707–718. [CrossRef]
38. Sałacińska, A.; Kusiak, M.A.; Whitehouse, M.J.; Dunkley, D.J.; Wilde, S.A.; Kielman, R. Complexity of the early Archean Uivak Gneiss: Insights from Tigigakyuk Inlet, Saglek Block, Labrador, Canada and possible correlations with south West Greenland. *Precambr. Res.* **2018**, *315*, 103–119. [CrossRef]
39. Kusiak, M.A.; Dunkley, D.J.; Whitehouse, M.J.; Wilde, S.A.; Sałacińska, A.; Konečný, P.; Szopa, K.; Gawęda, A.; Chew, D. Peak to post-peak thermal history of the Saglek Block of Labrador: A multiphase and multi-instrumental approach to geochronology. *Chem. Geol.* **2018**, *484*, 210–223. [CrossRef]
40. Dunkley, D.J.; Kusiak, M.A.; Wilde, S.A.; Whitehouse, M.J.; Sałacińska, A.; Kielman, R.; Konečný, P. Two Neoarchean tectonothermal events on the western edge of the North Atlantic Craton, as revealed by SIMS dating of the Saglek Block, Nain Province, Labrador. *J. Geol. Soc.* **2020**, *177*, 31–49. [CrossRef]
41. Wanless, R.; Bridgwater, D.; Collerson, K.D. Zircon age measurements for Uivak II gneisses from the Saglek area, Labrador. *Can. J. Earth Sci.* **1979**, *16*, 962–965. [CrossRef]

42. Collerson, K.D. Ion microprobe zircon geochronology of the Uivak gneisses: Implications for the evolution of early terrestrial crust in the North Atlantic Craton. In Proceedings of the Cross Section of Archean Crust, Ottawa, ON, Canada, 11−16 August 1983.
43. Baadsgaard, H.; Collerson, K.D.; Bridgwater, D. The Archean gneiss complex of northern Labrador. 1. Preliminary U–Th–Pb geochronology. *Can. J. Earth Sci.* **1979**, *16*, 951–961. [CrossRef]
44. Schiøtte, L.; Noble, S.; Bridgwater, D. U–Pb mineral ages from northern Labrador: Possible evidence for interlayering of Early and Middle Archean tectonic slices. *Geosci. Can.* **1990**, *17*, 227–231.
45. Schiøtte, L.; Compston, W.; Bridgwater, D. Ion probe U–Th–Pb zircon dating of polymetamorphic orthogneisses from northern Labrador, Canada. *Can. J. Earth Sci.* **1989**, *26*, 1533–1556. [CrossRef]
46. Wasilewski, B.; O'Neil, J.; Rizo, H.; Paquette, J.-L.; Gannoun, A.-M. Over one billion years of Archean crust evolution revealed by zircon U-Pb and Hf isotopes from the Saglek-Hebron complex. *Precambr. Res.* **2021**, *359*, 106092. [CrossRef]
47. Vezinet, A.; Thomassot, E.; Pearson, D.G.; Stern, R.A.; Luo, Y.; Sarkar, C. Extreme $\delta^{18}O$ signatures in zircon from the Saglek Block (North Atlantic Craton) document reworking of mature supracrustal rocks as early as 3.5 Ga. *Geology* **2019**, *47*, 605–608. [CrossRef]
48. Ryan, B.; Martineau, Y. Revised and coloured edition of 1992 map showing the Geology of the Saglek Fiord–Hebron Fiord area, Labrador (NTS 14L/2, 3, 6, 7). *Scale* **2012**, *1*. Available online: https://www.gov.nl.ca/iet/files/Map2012-15.pdf (accessed on 29 November 2021).
49. Bouvier, A.; Vervoort, J.D.; Patchett, P.J. The Lu–Hf and Sm–Nd isotopic composition of CHUR: Constraints from unequilibrated chondrites and implications for the bulk composition of terrestrial planets. *EPSL* **2008**, *273*, 48–57. [CrossRef]
50. Whitney, D.L.; Evans, B.W. Abbreviations for names of rock-forming minerals. *Am. Mineral.* **2010**, *95*, 185. [CrossRef]
51. Yang, Y.-H.; Wu, F.-Y.; Yang, J.-H.; Chew, D.M.; Xie, L.-W.; Chu, Z.-Y.; Zhang, Y.-B.; Huang, C. Sr and Nd isotopic compositions of apatite reference materials used in U–Th–Pb geochronology. *Chem. Geol.* **2014**, *385*, 35–55. [CrossRef]
52. Scrivner, A.E.; Vance, D.; Rohling, E.J. New neodymium isotope data quantify Nile involvement in Mediterranean anoxic episodes. *Geology* **2004**, *32*, 565–568. [CrossRef]
53. Vance, D.; Thirlwall, M. An assessment of mass discrimination in MC-ICPMS using Nd isotopes. *Chem. Geol.* **2002**, *185*, 227–240. [CrossRef]
54. Jochum, K.P.; Nohl, U.; Herwig, K.; Lammel, E.; Stoll, B.; Hofmann, A.W. GeoReM: A new geochemical database for reference materials and isotopic standards. *Geostand. Geoanal. Res.* **2005**, *29*, 333–338. [CrossRef]
55. Vermeesch, P. IsoplotR: A free and open toolbox for geochronology. *Geosci. Front.* **2018**, *9*, 1479–1493. [CrossRef]
56. Wendt, I.; Carl, C. The statistical distribution of the mean squared weighted deviation. *Chem. Geol. Isot. Geosci. Sect.* **1991**, *86*, 275–285. [CrossRef]
57. Ickert, R.B. Algorithms for estimating uncertainties in initial radiogenic isotope ratios and model ages. *Chem. Geol.* **2013**, *340*, 131–138. [CrossRef]
58. Rubatto, D. Zircon: The metamorphic mineral. *Rev. Mineral. Geochem.* **2017**, *83*, 261–295. [CrossRef]
59. Kirkland, C.; Yakymchuk, C.; Szilas, K.; Evans, N.; Hollis, J.; McDonald, B.; Gardiner, N. Apatite: A U-Pb thermochronometer or geochronometer? *Lithos* **2018**, *318*, 143–157. [CrossRef]
60. Cherniak, D. Rare earth element diffusion in apatite. *Geochim. Cosmochim. Acta* **2000**, *64*, 3871–3885. [CrossRef]
61. Cherniak, D.J.; Lanford, W.A.; Ryerson, F. Lead diffusion in apatite and zircon using ion implantation and Rutherford backscattering techniques. *Geochim. Cosmochim. Acta* **1991**, *55*, 1663–1673. [CrossRef]
62. Geisler, T.; Schaltegger, U.; Tomaschek, F. Re-equilibration of zircon in aqueous fluids and melts. *Elements* **2007**, *3*, 43–50. [CrossRef]
63. Harlov, D.E. Apatite: A fingerprint for metasomatic processes. *Elements* **2015**, *11*, 171–176. [CrossRef]
64. Putnis, A. Mineral replacement reactions. *Rev. Mineral. Geochem.* **2009**, *70*, 87–124. [CrossRef]
65. Krogh, T.E.; Kamo, S.L. Precise U–Pb zircon ID-TIMS ages provide an alternative interpretation to early ion microprobe ages and new insights into Archean crustal processes, northern Labrador. *Geol. Soc. Am. Spec. Papers* **2006**, *405*, 91–103.
66. Wasteneys, H.A.; Wardle, R.J.; Krogh, T.E. Extrapolation of tectonic boundaries across the Labrador shelf: U–Pb geochronology of well samples. *Can. J. Earth Sci.* **1996**, *33*, 1308–1324. [CrossRef]
67. Salerno, R.; Vervoort, J.; Fisher, C.; Kemp, A.; Roberts, N. The coupled Hf-Nd isotope record of the early Earth in the Pilbara Craton. *EPSL* **2021**, *572*, 117139. [CrossRef]
68. Sałacińska, A.; Kusiak, M.A.; Whitehouse, M.J.; Dunkley, D.J.; Wilde, S.A.; Kielman, R.; Król, P. Gneiss-forming events in the Saglek Block, Labrador; a reappraisal of the Uivak gneiss. *Int. J. Earth Sci.* **2019**, *108*, 753–778. [CrossRef]